

Design of compact integrated diamond nitrogen-vacancy center quantum probe

Sheng-Kai Xia(夏圣开), Wen-Tao Lu(卢文韬), Xu-Tong Zhao(赵旭彤), Ya-Wen Xue(薛雅文), Zeng-Bo Xu(许增博), Shi-Yu Ge(葛仕宇), Yang Wang(汪洋), Lin-Yan Yu(虞林嫣), Yu-Chen Bian(卞雨辰), Si-Han An(安思瀚), Bo Yang(杨博), Jian-Jun Xiang(向建军), and Guan-Xiang Du(杜关祥)

Citation: Chin. Phys. B, 2024, 33 (**5**): 054202. DOI: 10.1088/1674-1056/ad2bf6
Journal homepage: http://cpb.iphy.ac.cn; http://iopscience.iop.org/cpb

What follows is a list of articles you may be interested in

Versatile and controlled quantum teleportation network

Yao-Yao Zhou(周瑶瑶), Peng-Xian Mei(梅鹏娴), Yan-Hong Liu(刘艳红), Liang Wu(吴量), Yan-Xiang Li(李雁翔), Zhi-Hui Yan(闫智辉), and Xiao-Jun Jia(贾晓军)

Chin. Phys. B, 2024, 33 (**3**): 034209. DOI: 10.1088/1674-1056/ad1981

Engineering the spectra of photon triplets generated from micro/nanofiber

Chuan Qu(瞿川), Dongqin Guo(郭东琴), Xiaoxiao Li(李笑笑), Zhenqi Liu(刘振旗), Yi Zhao(赵义), Shenghai Zhang(张胜海), and Zhengtong Wei(卫正统)

Chin. Phys. B, 2024, 33 (**3**): 034208. DOI: 10.1088/1674-1056/ad1c5d

Thermometry utilizing stored short-wavelength spin waves in cold atomic ensembles

Xingchang Wang(王兴昌), Jianmin Wang(王建民), Ying Zuo(左瀛), Liang Dong(董亮), Georgios A Siviloglou, and Jiefei Chen(陈洁菲)

Chin. Phys. B, 2023, 32 (**7**): 074206. DOI: 10.1088/1674-1056/accb4f

Light slowing and all-optical time division multiplexing of hybrid four-wave mixing signal in nitrogen-vacancy center

Ruimin Wang(王瑞敏), Irfan Ahmed, Faizan Raza, Changbiao Li(李昌彪), Yanpeng Zhang(张彦鹏)

Chin. Phys. B, 2020, 29 (**5**): 054204. DOI: 10.1088/1674-1056/ab7b50

Laser-polarization-dependent spontaneous emission of the zero phonon line from single nitrogen–vacancy center in diamond

Zhang Duo (张多), Li Jia-Hua (李家华), Yang Xiao-Xue (杨晓雪)

Chin. Phys. B, 2014, 23 (**4**): 044204. DOI: 10.1088/1674-1056/23/4/044204

Design of compact integrated diamond nitrogen–vacancy center quantum probe

Sheng-Kai Xia(夏圣开)[1], Wen-Tao Lu(卢文韬)[2], Xu-Tong Zhao(赵旭彤)[3], Ya-Wen Xue(薛雅文)[4], Zeng-Bo Xu(许增博)[5], Shi-Yu Ge(葛仕宇)[3], Yang Wang(汪洋)[4], Lin-Yan Yu(虞林嫣)[3], Yu-Chen Bian(卞雨辰)[2], Si-Han An(安思瀚)[3], Bo Yang(杨博)[6], Jian-Jun Xiang(向建军)[7], and Guan-Xiang Du(杜关祥)[3,†]

[1] *School of Computer Science, Nanjing University of Posts and Telecommunications, Nanjing* 210023, *China*
[2] *Portland Institute, Nanjing University of Posts and Telecommunications, Nanjing* 210023, *China*
[3] *College of Telecommunications and Information Engineering, Nanjing University of Posts and Telecommunications, Nanjing* 210003, *China*
[4] *School of Science, Nanjing University of Posts and Telecommunications, Nanjing* 210023, *China*
[5] *School of Economics, Nanjing University of Posts and Telecommunications, Nanjing* 210023, *China*
[6] *Jiangsu Institute of Quality and Standardization, Nanjing* 210012, *China*
[7] *Chengdu Analog Circuit Technology Inc., Chengdu* 201203, *China*

(Received 27 December 2023; revised manuscript received 6 February 2024; accepted manuscript online 22 February 2024)

An integrated quantum probe for magnetic field imaging is proposed, where the nitrogen–vacancy (NV) center fixed at the fiber tip is located on the periphery of flexible ring resonator. Using flexible polyimide (PI) as the substrate medium, we design a circular microstrip antenna, which can achieve a bandwidth of 140 MHz at Zeeman splitting frequency of 2.87 GHz, specifically suitable for NV center experiments. Subsequently, this antenna is seamlessly fixed at a three-dimensional-printed cylindrical support, allowing the optical fiber tip to extend out of a dedicated aperture. To mitigate errors originating from processing, precise tuning within a narrow range can be achieved by adjusting the conformal amplitude. Finally, we image the microwave magnetic field around the integrated probe with high resolution, and determine the suitable area for placing the fiber tip (SAP).

Keywords: nitrogen–vacancy center, conformal antenna, integrated probe, magnetic field imaging

PACS: 42.50.Ex, 07.55.Ge, 03.65.Yz **DOI:** 10.1088/1674-1056/ad2bf6

1. Introduction

As a superior magnetic sensing platform, the negatively charged nitrogen–vacancy (NV) center in diamond has attracted extensive attention, primarily owing to its nano-scale spatial resolution and high magnetic sensitivity.[1–3] Using the optically detected magnetic resonance (ODMR) technology, the electron spin can be initialized, manipulated, and measured by using optical excitation and microwave,[4,5] which lays a foundation for quantum information processing and precision measurement.[6]

In conventional experiments, optical components such as objectives, lenses, and dichroic mirrors are employed to guide light for initialization and detection. However, this approach have the disadvantages of being bulky and inconvenient to carry.[7] In order to solve these problems, the idea of using optical fiber to excite the NV center in diamond and collect its fluorescence for optical fiber sensing has been proposed.[8–10] This innovative design opens up possibilities for reaching previously inaccessible fields in traditional NV-based sensors. An exemplary demonstration of this concept comes from the work of Dong[11] and Duan,[12] who introduced a diamond microcrystal containing a nitrogen vacancy center fixed at a fiber tip. The configuration showcases the symbiotic relationship between the NV center in diamond and the flexibility and compactness of the optical fiber.

In NV-based sensing systems, microstrip antennas and their various derivatives serve as prevalent microwave transmission technologies. The development trend of microstrip antenna for NV center is to broaden bandwidth[13] and control resonance through the change of physical size.[14,15] However, these designs are typically based on the concept of separating the optical fiber probe from the microwave antenna. Cumulative experience highlights several drawbacks: for one thing, owing to the thickness of the PCB board, an inevitable gap exists between the NV center and the sample, so the fiber diamond probe fails to be close enough to the device under test; for another, intricate adjustments are required for the precise positioning of the probe and antenna, increasing the risk of fracturing the fiber diamond probe.

In the present study, we demonstrate an integrated method that combines a fiber-optic probe with a flexible microstrip antenna, establishing a direct correlation between antenna size and resonant frequency. Our method is divided into the following three key steps:

(i) Design a circular patch antenna on a polyimide (PI) substrate with a resonant frequency of 2.87 GHz and a bandwidth of 140 MHz, which is tailored specifically for experiments involving NV center.

†Corresponding author. E-mail: duguanxiang@njupt.edu.cn

© 2024 Chinese Physical Society and IOP Publishing Ltd

(ii) Install the above flexible antenna onto a 3D-printed rigid support and integrate it with an optic-fiber coupled with diamond NV center to create a unified probe.

(iii) Conduct ODMR experiments to validate the antenna's efficacy in manipulating spin states. Carry out high-resolution scanning imaging on the plane near the integrated probe and determine the suitable area for optical fiber placement (SAP).

This method can contribute to achieving better efficiency in microwave field generation required in fiber diamond quantum sensor.

2. Basic theory and experimental setup

The diamond NV center, characterized by its distinctive fluorescence properties, arises from nitrogen atoms replacing carbon atoms and neighboring vacancies. It exists in a triplet state system with electron spin $S = 1$ ($m_s = -1, 0, +1$).[16,17] Figure 1(a) shows the outline of its energy level structure, and the Hamiltonian is defined as[18]

$$H = D \cdot S_Z^2 + E \cdot \left(S_X^2 - S_Y^2\right) - \gamma_e \cdot \boldsymbol{B} \cdot \boldsymbol{S}. \tag{1}$$

Here, $D = 2.87$ GHz is the room-temperature natural ground-state between sublevels $m_s = \pm 1$ and $m_s = 0$. Due to the difference in crystal strain and surface state among different diamond samples, the temperature-dependent parameter D ($\mathrm{d}D/\mathrm{d}T$) has different values.[19] The parameter D is typically determined through real-time Gaussian fitting of the sharp dip portion in the zero-field splitting ODMR spectrum.[20] E denotes the horizontal zero-field splitting coefficient, indicative of electric field strength. The stress field and electric field distribution can be deduced theoretically from changes in the E-value. Under the condition without external magnetic fields, the ground state $m_s = \pm 1$ is degenerate. In the presence of an external magnetic fields, the energy level $m_s = \pm 1$ undergoes Zeeman splitting,[21] where the electron spin magnetic ratio γ_e is 2.8 MHz/Gs (1 Gs = 10^{-4} T). $\boldsymbol{B}$ represents the applied magnetic field and $\boldsymbol{S}$ is the electron spin operator, with S_x, S_y, S_z being the components of $\boldsymbol{S}$ along the X, Y, Z axes, respectively. By using the crystal axis azimuth measurement method, the NV axis can be rotated to a specified direction, sensing the vector magnetic field component.[22]

Figure 1(b) gives the outline of key elements of experimental setup. The designed scanning magnetic imaging system comprises two primary modules:[23] an optical module and a control module. A 532-nm pulsed laser, mirrors, objective lens, an avalanche photon diode (APD) and other optical components are incorporated into an optical module, which is used to complete the transmission and conversion of optical signals. The control module consists of a pulse generator, a microwave signal source, a spectrum analyzer, and a computer to achieve data acquisition, analysis, and processing of optoelectronic signals. Additionally, a motorized displacement stages is used for implementing the micron scanning imaging.

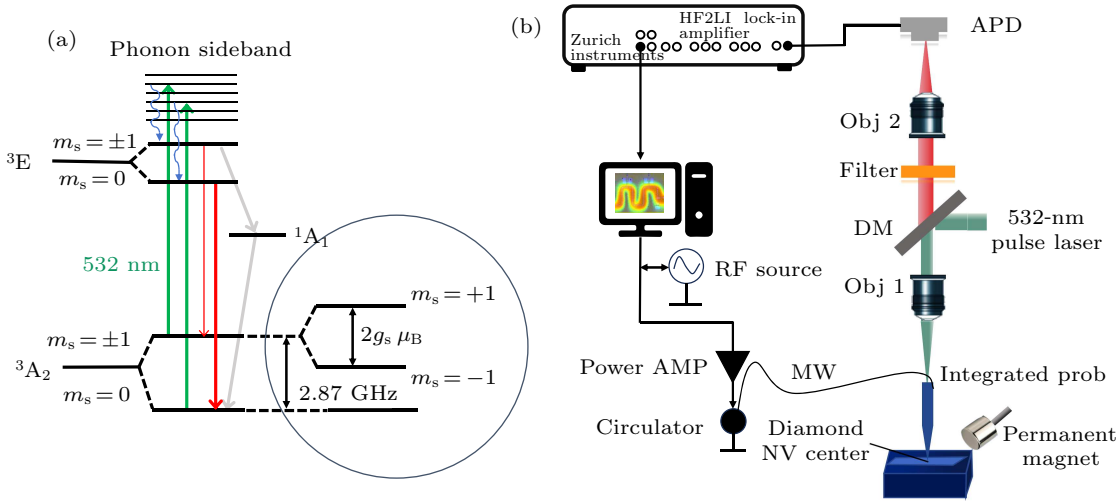


Fig. 1. (a) Energy diagram of diamond NV center and (b) schematic diagram of experimental setup.

The experimental procedure begins with the initialization of the NV center electron spin state through using a 532-nm green laser. A permanent magnet is used to induce the splitting of its magnetic sub-levels. When the microwave signal resonates with the energy level, a notable reduction in the fluorescence signal, corresponding to the energy gap between the two spin states, is observed on the oscilloscope. This technique can be used to accurately detect the resonant frequency relating to the ground state energy level of the NV center, which enables the inferring of the magnitude of the external magnetic field.

3. Simulation design of conformal antenna

The traditional microstrip antenna used for NV center experiment is based on printed circuit board (PCB). However, due to the inherent rigidity of the PCB material, it poses challenges in terms of space efficiency. Additionally, the dielec-

tric constant of the substrate undergoes variations with temperature changing. Notably, during the temperature ascending from 0 °C to 70 °C, the maximum fluctuation range can extend up to 20%, directly affecting the line delay and signal frequency.[24] In recent years, to meet the need to develop the miniaturization and high density of electronic products, a flexible PCB has emerged, which has the advantages of small size, lightweight and easy bending.[25] It is thermally stable at temperature of up to 280 °C for half an hour.

To fully utilize three-dimensional (3D) space, we devised a circular resonant antenna with polyimide (PI) substrate (thickness $h_1 = 0.1$ mm, dielectric constant $\varepsilon_r = 3.4$, tangent value of loss angle $\tan\delta = 0.005$). The entire process of designing the conformal antenna is depicted in Fig. 2. The left figure illustrates the planar structure of the antenna, with both the conductive patch and the grounding plane fabricated from electrolytic copper (thickness $h_2 = 0.0175$ mm). In contrast to ordinary ring resonators that solely possess patch holes, a through-hole has been incorporated in the central circular area, penetrating the patch layer, dielectric layer and ground layer, which facilitates the accommodation of an optical fiber extension. The right figure depicts the antenna being conformal around a cylindrical surface with a radius of r_3. Here, the cylinder and XY plane are tangent to the straight line $\begin{cases} X = -6 \text{ mm}, \\ Z = 0. \end{cases}$

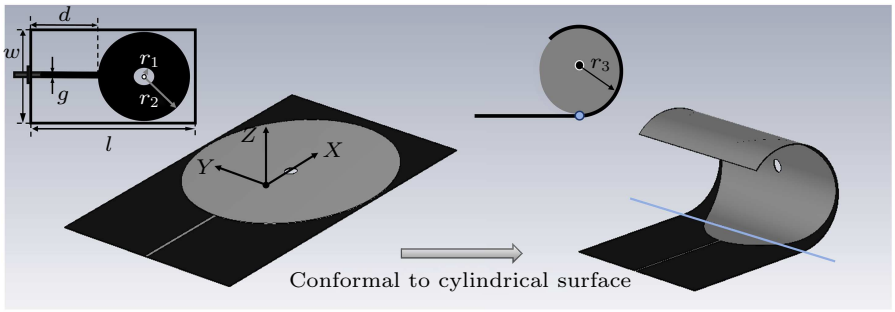


Fig. 2. Schematic diagram of antenna plane structure and conformal to cylindrical surface.

The full-wave numerical simulation (CST Microwave Studio V. 2022) results show that the resonant frequency of the flexible antenna undergoes minimal change under arbitrary bending conditions. Therefore, our approach involves the initial designing of the planar structure and the subsequent fine-tuning of the resonant frequency through bending. Given the zero-field splitting value of NV center as 2.87 GHz, the central frequency of microwave radiation needs to be around this frequency. The outer radius of the circular microstrip antenna can be obtained from the equation $f_r = c/2\pi r_2\sqrt{\varepsilon_r}$, where c represents the propagation velocity of electromagnetic wave in free space. Although the inner radius has little effect on the resonant frequency, we consider it to be at least 250 μm to facilitate the extension of the fiber. After performing frequency sweep analysis near the resonant frequency, we can obtain the geometric parameters listed in Table 1.

Table 1. Main parameters of the conformal antenna.

Parameter	Description	Value (mm)
l	length of FPCB	50
w	width of FPCB	34
h_1	substrate thickness	0.1
h_2	patch thickness	0.0175
d	length of rectangular patch	15
g	width of rectangular patch	0.6
r_1	inner radius of annular patch	1
r_2	outer radius of annular patch	16.5
r_3	radius of conformal cylindrical surface	8

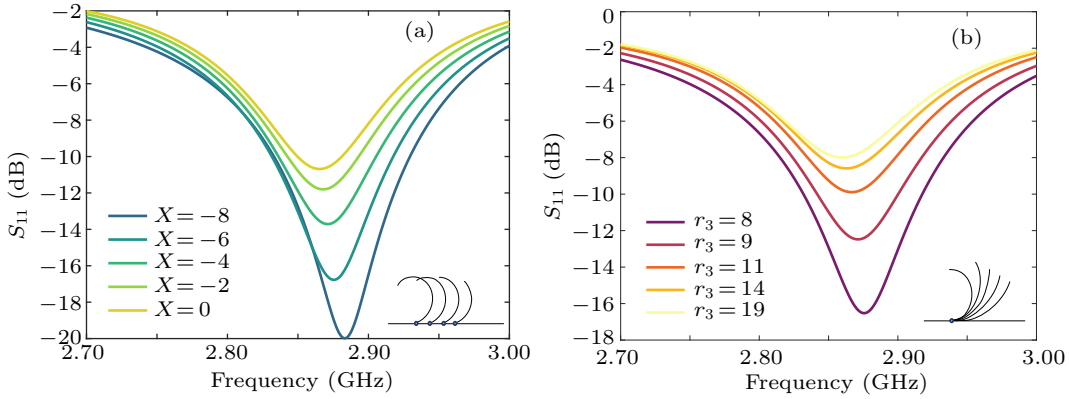


Fig. 3. The S_{11} parameters varying with frequency for (a) different tangent positions and (b) various values of support radius r_3.

The S parameter serves as a crucial metric for characterizing the transmission performance of an antenna. The S_{11} is defined as the input reflection coefficient of the antenna, specifically it is expressed as the ratio of the reflected voltage to the incident voltage. In our simulations, we use the control variable method to investigate the influence of the parameters x_1 and r_3 on the S_{11} curve as shown in Figs. 3(a) and 3(b) respectively. The resonant frequency will shift toward high frequency with the increase of conformal amplitude, but toward low frequency with the increase of conformal cylinder radius r_3. This insightful analysis provides a foundation for manually adjusting the resonant frequency of the flexible antenna.

4. Characterization of integrated probe

Figure 4(a) displays a physical map of the flexible antenna fed by a coaxial line. The inner conductor is connected to the antenna's feeder, and the outer conductor is linked to the grounding pad for reference. Figure 4(b) illustrates the printing bracket, featuring a cleverly designed card slot that accommodates the flexible antenna. This setup allows the antenna to be seamlessly fitted on the bracket's surface and move in the direction indicated by the gray arrow. The integrated probe's final diagram, along with its internal structure, is presented in Fig. 4(c). Notably, the design enables the protruding optical fiber to approach the surface of the device under test with unparalleled proximity. This advancement eliminates the previous limitations imposed by the thickness of the PCB board.

In the experiment, our primary effort is to evaluate the return loss of the antenna and its ability to radiate electromagnetic waves. We use a vector network analyzer (Ceyear-3672D, 10 MHz–50 GHz) to measure S_{11}. As shown in Fig. 4(d), when the frequency range is set to 2.7 GHz–3.0 GHz, the comparison between numerical simulation results and experimental data shows that they are in good agreement with each other. The minor deviation may be attributed to the line error of ± 0.02 mm and the shape tolerance of ± 0.1 mm during processing. The minimum value of S_{11} in the measurement results is -14.841 dB, indicating that the antenna has achieved good impedance matching and low return loss.

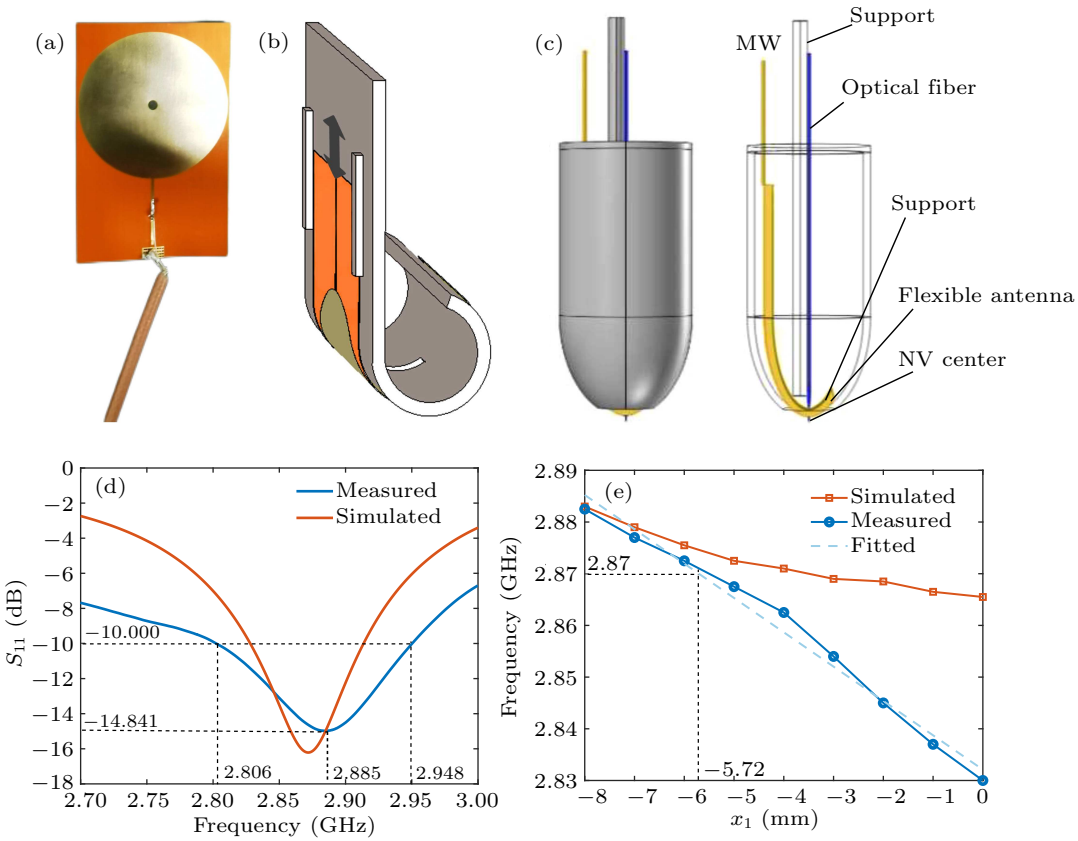


Fig. 4. (a) Physical map of flexible antenna. (b) Schematic diagram of antenna conformal to 3D printing resin bracket, with gray arrow indicating conformal amplitude adjusted manually. (c) Conceptual diagram and internal detailed structure of the integrated probe. (d) Frequency-dependent S_{11} parameters of conformal antenna. (e) Simulation results and experimental results of manual tuning in Fig. 4(b).

In order to use the microwave resonator for ODMR applications, it is critical to align its resonant frequency with NV center's ESR frequency. Traditional resonant rings generally adjust the resonant frequency by changing the size of the radius (r_2), often necessitating multiple iterations to attain the desired resonance. Contrarily, our innovatively designed flexible antenna facilitates minor adjustments in resonance by modulating the conformal amplitude on the supporting struc-

ture as elucidated by the gray arrow in Fig. 4(b). Figure 4(e) sketches the effect of modifying the tangent position on the resonant frequency. The test results show that the resonant frequency can vary from 2.830 GHz to 2.882 GHz by changing X from 0 mm to −8 mm. Furthermore, a nearly linear relationship exists between the resonant frequency and the inner cavity radius, characterized by a slope of approximately −2.28 MHz/mm.

Prior to initiating the ODMR experiment, we utilize the subcarrier modulation mechanism[11] to modulate three TTL signals: laser (ON/OFF = 500 ns/1500 ns), microwave (On = 1450 ns), and subcarrier (ON/OFF = 1.78 ms/1.78 ms), as depicted in Fig. 5(a) with $N = 890$. In the frequency domain, the pulsed fluorescence exhibits a frequency component (V_c) at 0.5 MHz, and modulation produces a sideband signal (V_s) of the fluorescence carrier signal. The ratio of V_s to V_c, known as the modulation depth,[11] serves as an indicator in Fig. 5(b).

The presence of an external static magnetic field triggers off the Zeeman splitting of the diamond NV center, manifested by dividing a single spectral peak into multiple peaks in the ODMR spectrum. Assuming that the diamond NV center possesses four NV axes, each with different two-state transitions, the ODMR spectrum displays a total of eight non-overlapping peaks. To analyze the data, a Lorentz function can be used for fitting the original data points, which is expressed as

$$S(A, w, f_0) = \frac{Aw^2}{(f - f_0)^2 + w^2}, \tag{2}$$

where S is the actually detected signal amplitude, A the peak intensity of the resonant absorption peak, $2w$ the full width at half maximum, f the microwave frequency, and f_0 the center frequency of the resonant peak.

Following the ODMR experiment, our focus shifts toward characterizing the near-field radiation of the antenna. This involves scanning the microwave magnetic field point by point to pinpoint the suitable area for fiber placement (SAP). The highlighted blue area (BA) depicted in Fig. 5(c), situated approximately 50 μm above the integrated probe, is chosen as the target for investigation. Figure 5(d) illustrates the surface magnetic field distribution of the BA, obtained via CST software simulation, with the data normalized for visual analysis. To experimentally determine the microwave magnetic field strength, Rabi measurement and fitting for each position in this region are required, a process that can be time-intensive. In the case where the microwave action duration is notably brief, the detected fluorescence signal intensity at the sideband frequency exhibits a nearly linear relationship with the microwave field strength.[11] A more time-efficient approach involving characterizing the microwave magnetic field intensity through the fluorescence intensity generated, which is accomplished by reducing the duration of the microwave pulse.

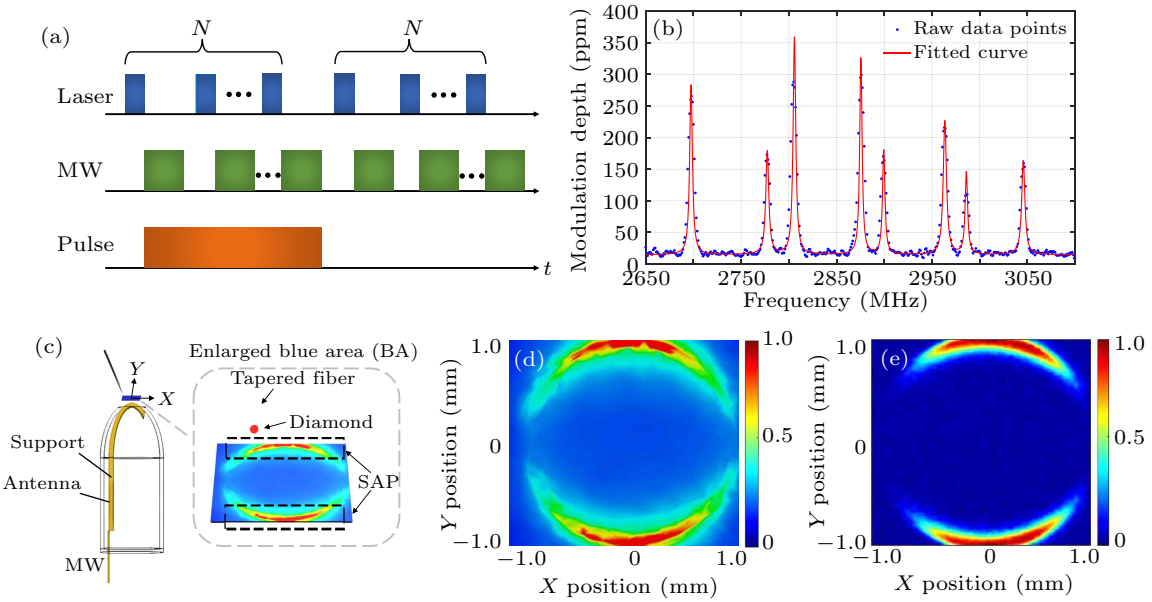


Fig. 5. (a) System pulse sequence, (b) ODMR measurement and curve fitting, (c) schematic diagram of scanning imaging and *XY* coordinate system, with BA representing the plane to be scanned, and SAP denoting the area where the microwave field is concentrated, (d) simulation results of magnetic field distribution, and (e) experimental scanning results of magnetic field distribution.

Using precise control via LABVIEW software, we conduct meticulous scanning of the BA with a 2-mm side length, employing steps as fine as 0.62 μm. Figure 5(e) illustrates the measured distribution characteristics of the microwave magnetic field on the BA, with the data normalized. The experimental results are in good agreement with the simulation results, indicating that the microwave magnetic field primarily occupies a slender and elongated region measuring

0.6 mm×0.1 mm along the periphery of the hole.

In order to further determine the field strength near the aperture, we conduct simulations to evaluate the magnetic field size in both lateral direction and axial direction of the integrated probe. Figure 6(a) shows the variation of field strength along the Y-axis direction in the BA plane. At a microwave power of 30 dBm, the field strength exceeds 1 Gs at a distance of 100 μm from the edge of the hole and 0.5 Gs at a distance of 200 μm from the edge.

To investigate the B-field axial attenuation, we place the diamond near the P-point at the edge of the hole (∼ 0.1 mm away). Starting from the BA plane, our examination entails meticulous scanning along the Z axis in steps of 0.1 mm. We normalize the data and employ least squares fitting for precise analysis, and the results are shown in Fig. 6(b). A comparison with simulation results reveals a similar attenuation pattern: initially decreasing gradually, then rapidly decreasing, and finally stabilizing. Considering the BA's selected height (∼ 50 μm) and the presence of the B-field (∼ 1 Gs) 20 μm ahead of the BA, sufficient to excite the NV center, this approach reaffirms the feasibility of the flexible antenna design. After determining the SAP and Z-axis attenuation, the optical fiber, coupled with the NV center, is enclosed in the antenna and bracket as depicted in Fig. 4(c).

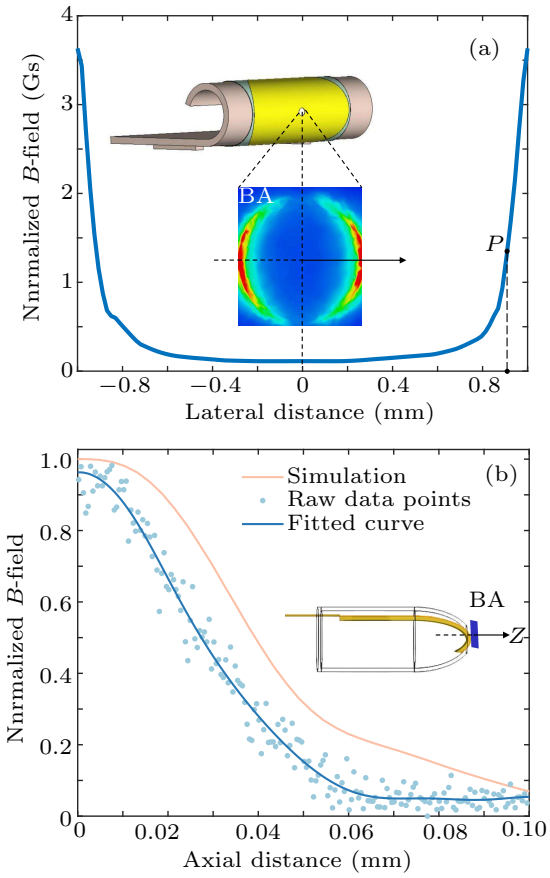


Fig. 6. (a) Simulated magnetic field intensity variation along the Y-axis lateral distance in BA plane and (b) variations of axial magnetic field intensity with axial distance in vertical BA plane.

5. Conclusions and perspectives

In response to the current trend of miniaturization and portability of quantum sensors, we introduced a novel, lightweight, and compact probe that integrates optical fiber and microwave antenna. Taking full advantage of the characteristics of FPCB, we designed a circular microstrip antenna with a resonant frequency of 2.87 GHz and a bandwidth of 140 MHz. When conforming the flexible antenna to a 3D-printed bracket, we can achieve linear tuning (slope: −2.28 MHz/mm) within a range of 50 MHz by adjusting the conformal amplitude. The central region of the antenna features a through-hole designed to host the fiber diamond, ensuring close proximity of the diamond NV center to the surface of the device under test. Establishing a scanning plane in approximately 50 μm away from the integrated probe, we employ the optical fiber quantum probe for high-resolution imaging of the microwave magnetic field in a 2 mm×2 mm area (BA). The experimental data and simulation results both indicate that there is a strong microwave magnetic field at the edge of the circular hole. Under an applied microwave power value of 30 dBm, the magnetic field strength exceeds 1 Gs in a proximity of 100 μm away from the edge of the hole. So far, we have determined a suitable area (about 0.6 mm×0.1 mm) for placing the optical fiber tip (SAP).

The integrated probe we have designed possesses potential applications in both magnetic field and temperature sensing. In the past, extensive efforts have been devoted to the design and optimization of microstrip antenna patch shapes, primarily based on PCB boards. These established shapes, such as the circular patch exemplified here, can be seamlessly incorporated into our flexible antenna patch design. This approach offers novel perspectives for advancing the integration and flexibility of quantum sensors.

Acknowledgements

Project supported by the National Key Research and Development Program of China (Grant No. 2021YFB2012600) and the Science and Technology Plan Project of State Administration of Market Regulation, China (Grant No. 2021MK039).

References

[1] Balasubramanian G, Chan I Y, Kolesov R, Al-Hmoud M, Tisler J, Chang S, Kim C, Wojcik A, Hemmer P R and Krueger A 2008 *Nature* **455** 648
[2] Taylor J M, Cappellaro P, Childress L, Jiang L, Budker D, Hemmer P R, Yacoby A, Walsworth R and Lukin M D 2008 *Nat. Phys.* **4** 810
[3] He W H, Dong M M, Hu Z Z, Zhang Q H, Yang B, Liu Y, Fan X L and Du G X 2019 *Chin. Phys. Lett.* **36** 127601
[4] Gurudev Dutt M V, Childress L, Jiang L, Togan E, Maze J, Jelezko F, Zibrov A S, Hemmer P R and Lukin M D 2007 *Science* **316** 1312
[5] Lifshitz E, Kaplan A, Ehrenfreund E and Meissner D 1999 *Chem. Phys. Lett.* **300** 626

[6] Wrachtrup J and Jelezko F 2006 *J. Phys.: Condens. Matter* **18** S807
[7] Gao Y, Zeng Y, Cui M M, Qiao Y Y, Yang X, Lin C N, Zhao J L, Li L, Wang Y and Shan C X 2022 *IEEE Transactions on Instrumentation and Measurement* **71** 1
[8] Rabeau J R, Huntington S T, Greentree A D and Prawer S 2005 *Appl. Phys. Lett.* **86** 134104
[9] Bai R X, Yang F, Liu P, Gao T R, Zhou L, Yin X H, Zhu X Y, Ma W H, He F Y, Chen N C, Sun Y, Ma J T, Yu T and Du G X 2022 *Appl. Phys. Lett.* **120** 044003
[10] Fedotov I V, Doronina-Amitonova L V, Voronin A A, Levchenko A O, Zibrov S A, Sidorov-Biryukov D A, Fedotov A B, Velichansky V L and Zheltikov A M 2014 *Sci. Rep.* **4** 5362
[11] Dong M M, Hu Z Z, Liu Y, Yang B, Wang Y J and Du G X 2018 *Appl. Phys. Lett.* **113** 131105
[12] Duan D, Du G X, Kavatamane V K, Arumugam S, Tzeng Y K, Chang H C and Balasubramanian G 2019 *Opt. Express* **27** 6734
[13] Sasaki K, Monnai Y, Saijo S, Fujita R, Watanabe H, Junko I H, Itoh K M and Abe E 2016 *Rev. Sci. Instrum.* **87** 053904
[14] Matin M A and Sayeed A I 2010 *WSEAS Transactions on Communications* **9** 63
[15] Bayat K, Choy J, Farrokh Baroughi M, Meesala S and Loncar M 2014 *Nano Lett.* **14** 1208
[16] Doherty M W, Manson N B, Delaney P, Jelezko F, Wrachtrup J and Hollenberg L C L 2013 *Phys. Rep.* **528** 1
[17] Yang B, Dong Y, Hu Z Z, Liu G Q, Wang Y J and Du G X 2018 *IEEE Transactions on Microwave Theory and Techniques* **66** 2276
[18] Steiner M, Neumann P, Beck J, Jelezko F and Wrachtrup J 2010 *Phys. Rev.* **81** 035205
[19] Sunuk C, Jungbae Y, Myeongwon L, Jooeon O, Dongkwon L, Heeseong K, Chul-Ho L and Donghun L 2018 *Current Appl. Phys.* **18** 1066
[20] Yang H, Chen G B, Zhao X T, He F Y and Du G X 2023 *IEEE Sensors Journal* **23** 28633
[21] Hu C M, Nitta J, Akazaki T, Takayanagi H, Osaka J, Pfeffer P and Zawadzki W 1999 *Phys. Rev.* **60** 7736
[22] Chen G B, Gu B X, He W H, Guo Z G and Du G X 2020 *IEEE Journal of Quantum Electronics* **5** 1
[23] Bai R X, Zhu X Y, Yang F, Gao T R, Wang Z R, Yu L Y, Wang J F, Zhou L and Du G X 2022 *Chin. Phys. B* **31** 074203
[24] Zhang H W, Liu Y, Wang J and Sun F L 2015 *Microelectronics Reliability* **55** 2391
[25] Lim C H, Abdullah M Z, Azid I A and Abdul Aziz M S 2017 *Microelectronics Reliability* **72** 5